Available online at www.sciencedirect.com

ScienceDirect

journal homepage: www.elsevier.com/locate/he

Reduced graphene oxide supported hierarchical flower like manganese oxide as efficient electrocatalysts toward reduction and evolution of oxygen

Srabanti Ghosh [a,*], *Prasenjit Kar* [a,1], *Nimai Bhandary* [b,1], *Suddhasatwa Basu* [b], *Thandavarayan Maiyalagan* [c], *Samim Sardar* [a], *Samir Kumar Pal* [a]

[a] *Department of Chemical, Biological and Macromolecular Sciences, S. N. Bose National Centre for Basic Sciences, Block JD, Sector III, Salt Lake, Kolkata, 700 098, India*

[b] *Chemical Engineering Department, Indian Institute of Technology Delhi, Hauz Khas, New Delhi, 110016, India*

[c] *SRM Research Institute, Department of Chemistry, SRM University, SRM Nagar, Potheri, Kattankulathur, 603 203, India*

ARTICLE INFO

Article history:
Received 17 August 2016
Received in revised form
29 November 2016
Accepted 1 December 2016
Available online 23 December 2016

Keywords:
Mn_2O_3
Reduced graphene oxides
Bifunctional electrocatalysis
Oxygen reduction reaction
Oxygen evolution reaction

ABSTRACT

The slow kinetics of the electrochemical oxygen reduction reaction (ORR) is a major bottleneck for the development of alkaline fuel cells. Herein, a facile and effective hydrothermal route has been developed to synthesize hierarchical with controllable structures of manganese oxides (Mn_2O_3) and reduced graphene oxides supported Mn_2O_3 composites. The hierarchal metal oxides were formed by self-assembly of very small Mn_2O_3 nanoparticles as evident from transmission electron microscopy. The nature of chelating agents has found to be the key factor whose subtle variation can effectively control the morphology of the Mn_2O_3. Electrochemical investigations indicate that the both pure and supported Mn_2O_3 demonstrate bifunctional catalytic activity toward the four-electron electrochemical reduction of oxygen and evolution reaction in alkaline media. Due to the 3D assembled hierarchical architecture of Mn_2O_3 composed of rose- and petal-like nano-particle arrays and the interconnection of reduced graphene oxides (rGO) network, as well as the synergetic effects of rGO as a support, revealing the pronounce impact on the electrocatalytic activity the Mn_2O_3 composites with high current density and excellent durability as cathode material which is comparable with other electrocatalysts. The synthetic approach provides a general platform for fabricating well-defined pure and supported metal oxides with prospective applications as low-cost catalysts for alkaline fuel cells.

* *Corresponding author.*
E-mail address: ghosh.srabanti@gmail.com (S. Ghosh).
[1] Equally contributed.

http://dx.doi.org/10.1016/j.ijhydene.2016.12.008
0360-3199/

Introduction

The superior efficiency of fuel-cell to converts chemical energy directly into electrical energy with low emission of pollutants makes a potentially viable option as an alternative future power source [1]. However, technological hurdles that still prevent the commercialization of fuel cell technologies require designing of low-cost, durable and nonprecious metal catalysts as alternatives to the bench marked Pt-based materials [2,3]. Recently, the excellent structural versatility of manganese oxides, which include MnO, MnO_2, Mn_2O_3, and Mn_3O_4, have received considerable interest for wide range applications in catalysis, energy storage in lithium ion batteries and fuel cells [4–6]. In this regards, the possibility of improving electrochemical properties by tailoring morphologies and surface structures, enormous effort is therefore devoted to developing morphology-controllable synthesis, however, suffer from the requirements of high temperature and tedious process [7–10]. Emerging research trends focus on hydrothermal synthesis as a rapid and facile route for metal oxide catalysts, however, only a few Mn_2O_3 porous structures having enhanced electrochemical performances, including high capacity, good cycling stability, and rate capability, as cathode materials reported till date [11,12]. Very recently, rapid synthesis of Mn_2O_3 microspheres using a hydrothermal approach has been reported by our group [13]. However, the role of structure controlling agent during hydrothermal synthesis in order to tune morphology of metal oxides structures is not addressed. Recently, the assembly of metal oxide molecules into three-dimensional (3D) hierarchical microstructured materials have attracted considerable interest because of multiphase heterogeneous interfaces, controllable physical and chemical microenvironment, high surface area, optimized pore size distribution and abundance of inner voids provides improved performance towards their potential application such as catalysts, super capacitors and solar cells etc [14–16]. Hence, it is crucial to develop facile routes for controlled formation of 3D hierarchical structures and assembly of complex nanostructures at low cost which still remains a challenge. One feasible approach is the synthesis of oxides materials using porous matrix as conductive support or template such as carbon nanotubes, metal–organic frameworks (MOFs) etc via a simple calcinations with controlled composition and microstructure on the nanoscale [17–19]. In particular, hierarchical structures, which are assembled by oxides materials and combined with electronically conductive agents, for example, carbon nanofibers, carbon nanotubes, conducting polymers, graphene, reduced graphene oxide (rGO) sheets have attracted a considerable attention [20–24]. In comparison to other supports, graphene sheets have been aroused great promise because of its excellent electrical conductivity, high surface area (calculated value = 2630 $m^2 g^{-1}$), as well as chemical stability [25,26]. Hence, graphene functionalized metal oxides as electrode materials have many advantages such as high surface area, preventing the aggregation of catalysts, possess good electrical conductivity to facilitate electronic transfer, offering easy access of the electrolyte to the electrode surface, allowing increased utilization of active material and enhanced stability [27]. Moreover, doped graphene oxides can be also used as efficient electrocatalysts having large number active sites generated from doping [28]. Here, we have designed a series of hierarchical transition metal oxides based microstructure supported on graphene nanosheets via one pot hydrothermal route for the electrooxidation of water.

Bifunctional catalysis is a novel concept in modern energy technologies, where the catalyst can be used for water splitting with oxygen evolution reactions (OER) as well as oxygen reduction reactions (ORR) during energy conversion between fuel and electricity [29,30]. The various electrochemical devices, fuel cells and metal–air batteries, direct solar or electricity-driven water splitting operates via electrochemical reactions involving oxygen supplied from the ambient air on the cathode, i.e., the oxygen reduction reaction during discharge and the oxygen evolution reaction during charge [31,32]. There has been extensive research on electro-catalytic materials that are capable of promoting both the ORR and the OER, however, transition metal oxides has been extensively used as alternative low cost, excellent electrocatalytic activity and high stability [33–38]. Dai and coworkers deposited Co_3O_4 nanoparticles on a graphene support and investigated their electrocatalytic activity [34]. Lee et al. developed a multistep process for the synthesis of highly efficient oxygen reduction electrocatalyst based on nitrogen-doped (N-doping) graphene nanosheets (NG) using mussel-inspired dopamine as a nitrogen source [35]. It has been proposed that N-doping may leads to improve catalytic activity as well as provides anchoring sites for the growth of manganese oxide nanowires on the graphene nanosheets (NG/MnOx). However, there is a contradiction about the role of doping in graphene nanosheets which may causes structural destabilization and make them prone to oxidation. Kokoh et al. also reported low oxide mass loading (ca. 30 wt %) Co_3O_4/nitrogen doped graphene-based composites as efficient electrocatalysts for ORR and OER [36]. In order to improve the electrochemical performance of metal oxides, further a series of mixed metal oxides have also been coupled with reduced graphene oxide as a highly active and stable bifunctional electrocatalyst [37–41]. Recently, Xu and co-workers development a high performance Au/$NiCo_2O_4$ based OER catalysts supported on the three-dimensional hierarchical porous graphene-like (3D HPG) material by ion-exchange/activation combination method using a metal ion exchanged resin as carbon precursor [42]. Very recently, Kannan et al. employed 3D graphene-mixed metal oxide-supported carbon palladium quantum dot nanoarchitectures as a bifunctional electrocatalyst for direct ethylene glycol fuel cells and oxygen evolution reactions [43]. However, the high cost and limited availability of Pt, Pd and Au metals are key barriers to the development of large scale oxygen catalysts using Pt-based, Pd-based and Au-based catalysts. Alternatively, Wen et al. reported reduced graphene oxide supported chromium oxide hybrid as a promising low cost and highly efficient catalyst for ORR by the pyrolysis of chromium-urea coordination compound [44]. Manganese oxides supported on graphene have also been employed as active, stable and low-cost electrocatalysts for fuel cells and Li–air batteries [45]. Kim and coworkers reported ionic liquid mediated Mn_3O_4 supported on graphene sheets as efficient ORR electrocatalysts with tunable oxygen reduction pathway [46]. Qiao et al. also developed a mesoporous Mn_3O_4/graphene hybrid

material which illustrates stable and high ORR catalytic activity [47]. In spite of huge attempt have been made to developed transition metal oxides based hybrid catalysts, reports regarding hierarchical Mn_2O_3/graphene hybrid materials using one pot synthesis is very limited. For the first time, we developed a facile and effective, one pot hydrothermal-assisted route for the synthesis of hierarchical, porous and electrochemically active graphene supported manganese oxide hybrid materials. Consequently, this simple synthetic methodology is a viable approach in making manganese oxide nanostructure as a highly active catalyst which can be extended for other metal oxides for application in fuel cells. Here, we report the controlled synthesis of pure and graphene supported Mn_2O_3 by a hydrothermal process exploring the role common chelating agents and their electrochemical behavior for ORR and OER in alkaline medium. These newly fabricated Mn_2O_3 microstructures were extensively characterized by using a wide range of methods including transmission electron microscopy, scanning electron microscopy, X-ray diffraction and thermal analysis.

Materials and methods

Materials

Manganese acetate dihydrate, polyvinyl alcohol, n-Trioctylphosphine oxide (TOPO, 99%), graphite powder, nafion were purchased from Sigma Aldrich. Ethylene glycols (EG) and absolute alcohol were obtained from Merck. All other chemicals employed were of analytical grade and used without further purification.

Synthesis of Mn_2O_3

In a typical procedure, 0.03 mol of manganese acetate dihydrate, and 0.05 mol of polyvinyl alcohol or 0.12 mol of n-trioctylphosphine oxide were dissolved 30 mL ethylene glycol. The resultant mixture was continuously stirred for 2 h to form a homogeneous solution and then transferred into a 30 mL Teflon-lined stainless-steel autoclave. The autoclave was sealed and maintained at 180 °C for 6 h for both polyvinyl alcohol and n-trioctylphosphine oxide. Then it was naturally cooled to ambient temperature. The final products were collected and washed with absolute alcohol three times. Then as-prepared samples were further annealed at 450 °C for 6 h under air atmosphere and black products were obtained.

Synthesis of Mn_2O_3 supported on reduced graphene oxide

The graphene oxide (GO) was synthesized from graphite powder by the modified Hummers method as reported in our previous publication [26,48]. The GO (0.5 mg mL^{-1}) was then dispersed in EG and exfoliated in an ultrasonic bath for 30 min. Then 0.03 mol of manganese acetate dihydrate, and 0.05 mol of polyvinyl alcohol or 0.12 mol of n-trioctylphosphine oxide was added to the GO dispersion. Then the mixture was loaded into a 30 mL Teflon-lined stainless-steel autoclave and heated at elevated temperature for several hours (at 180 °C for 6 h). Then as-prepared samples were further annealed at 450 °C for 6 h under air atmosphere and the samples were then washed with water and ethanol, and dried. The reduced GO was synthesized following the same procedure without adding the manganese salt. In an another set, 0.03 mol of manganese acetate dehydrate and GO were added into 30 mL ethylene glycol to prepare Mn_2O_3 without using PVA or TOPO. To investigate the morphology effect of the as-prepared Mn_2O_3 on the ORR performance, PVA, and TOPO have been used to control the Mn_2O_3 structure in presence and absence of graphene support by keeping other conditions the same and these samples are denoted as Mn_2O_3/PVA, Mn_2O_3/TOPO, Mn_2O_3/PVA/rGO and Mn_2O_3/TOPO/rGO.

Characterization

Transmission electron microscopy (TEM) grids were prepared by applying a diluted drop of the Mn_2O_3 samples to carbon-coated copper grids. Field Emission Scanning Electron Microscopy (FESEM, QUANTA FEG 250) investigations were performed by applying a diluted drop of Mn_2O_3 and rGO supported Mn_2O_3 samples on silicon wafer. The phase structures of the as-prepared samples were determined by powder X-ray diffraction (XRD, PANalytical XPERTPRO diffractometer equipped with Cu Kα radiation at 40 mA and 40 kV, a scanning rate of 0.02° S^{-1} in the 2θ range from 20° to 80°). Thermal gravimetric analysis (TGA) of Mn_2O_3 solid powder was performed under nitrogen atmosphere with a heating rate of 10 °C-min from 30 °C to 1000 °C by using a Perkin–Elmer TGA-50H.

Electrochemical test

Electrochemical RDE measurements were performed in a standard three-electrode glass cell on a using RRDE-3A Rotating Ring Disk Electrode Apparatus (BioLogic Science Instruments, France) connected to DY2300 potentiostat (Digi-Ivy Inc., USA) with a scan rate of 10 mV/s and potential range from 0 to 1 V for ORR under ambient conditions. Cyclic voltammetry (CV) and Chronoamperometry (CA) were performed for ORR and OER using a potentiostat galvanostat (SP150, BioLogic Science Instruments, France). A Pt wire and an Ag/AgCl/KCl (Sat. KCl) were used as counter and reference electrodes, respectively and 0.1 M KOH was used as an electrolyte. High-purity O_2 gas was purged for 30 min before each RDE experiment to make the electrolyte saturated with O_2. Catalyst ink was prepared by ultrasonically mixing 6.0 mg of Mn_2O_3 sample with 3 mL of pure deionized water and 10 μL of 5 wt% Nafion for 1 h in order to make a homogeneous suspension. Then, 5 μL of prepared catalytic ink was transferred to the surface of a glassy carbon electrode of 3 mm diameter as a working electrode. Finally, the ink was allowed to dry under ambient conditions. To evaluate the electrochemical activity for the oxygen evolution reaction (OER) of the Mn_2O_3, CV were performed under saturated N_2 solution. Pt wire and Ag/AgCl (Saturated KCl) were used as counter and reference electrodes, respectively and 0.1 M KOH was used as an electrolyte [29].

Electrochemical characterization was conducted using a single potentiostat with a scan rate of 10 mV s^{-1} and potential range from 0 to 1 V. Ink was prepared according to the method described above for ORR. The overall electron transfer numbers per oxygen molecule involved in the typical ORR process were calculated from the slopes of the Koutecky–Levich plots using the following equation [49]:

$$\frac{1}{j} = \frac{1}{j_L} + \frac{1}{j_K} = \frac{1}{B\omega^{\frac{1}{2}}} + \frac{1}{j_K} \quad (1)$$

$$B = 0.62\, nFC_0 (D_0)^{\frac{3}{2}} \nu^{-\frac{1}{6}} \quad (2)$$

$$j_K = nFk\, C_0 \quad (3)$$

where, j (mA/cm^2) is the measured current density, j_K and j_L (mA/cm^2) are the kinetic- and diffusion-limiting current densities, ω is the electrode rotating speed in rpm, n is the number of electrons transferred per oxygen molecule, F is the Faraday constant (F = 96485 C mol^{-1}), C_0 is the bulk concentration of O_2 (1.2×10^{-6} mol cm^{-3}), D_0 is diffusion coefficient of O_2 (1.9×10^{-5} cm^2 s^{-1}), ν is the kinematic viscosity of the electrolyte (0.01 cm^2 s^{-1}), and k is the electron transfer rate constant, respectively [49].

In-situ-FTIR study was carried out using a FTIR spectrometer (Bruker Vertex 70v) which is connected to a potentiostat galvanostat (PGSTAT30, AUTOLAB).

Oxygen can be directly reduced to water with the concomitant consumption of four electrons per O_2 molecule (Equation (4)). Alternatively, oxygen can be reduced indirectly, forming H_2O_2 as an intermediate and only two electrons per O_2 molecule are consumed (Equation (5)):

$$O_2 + 2H_2O + 4e^- \rightarrow H_2O + 4OH^- \quad (4)$$

$$O_2 + 2H_2O + 2e^- \rightarrow H_2O_2 + 2OH^- \quad (5)$$

Results and discussion

Characterization of Mn_2O_3

A facile and mild hydrothermal route has been used to synthesize Mn_2O_3 without the use of any template. The crystal structures and formation of the manganese oxides and graphene supported hybrid composites have been verified by powder X-ray diffraction. Typical XRD patterns of the as-prepared Mn_2O_3/PVA, Mn_2O_3/TOPO, Mn_2O_3/PVA/rGO and Mn_2O_3/TOPO/rGO are shown in Fig. 1. The peaks in the XRD patterns of the as-prepared manganese oxides can be well indexed to the (211), (222), (321), (311), (332), (400), (431), (440), (521), (541), (611), (622), (631) and (721) planes of the cubic phase Mn_2O_3 crystal (JCPDS No. 41-1442) indicating that they are all well-crystallized. These results are in consistent with our previous reports. For the hybrid sample, in addition to the peaks from Mn_2O_3 phase, there is additional diffraction peaks located at 2θ = 26.0° which can be attributed to the (002) reflection of reduced GO sheets (JCPDS No. 75-1621). In the Mn_2O_3/PVA/rGO and Mn_2O_3/TOPO/rGO, the diffraction peaks can be indexed as the planes of cubic phase Mn_2O_3 crystal and the broad diffraction peak at 26.0° corresponds to the (002) plane of the graphitic carbon, and indicates the presence of reduced graphene. Thus, XRD patterns indicate that Mn_2O_3 successfully incorporated on rGO layers. No other impurity peaks have been detected in both cases and the results confirm the successful formation of highly crystalline pure Mn_2O_3 over the rGO nanosheets by the present hydrothermal process.

The thermogravimetric (TG) data for the thermal decomposition of the Mn_2O_3 samples are shown in Fig. 1b. TG analysis of Mn_2O_3 powder showed a weight loss ~8% at 580 °C should be attributed to the removal of surface-adsorbed water which is consistent with previous reports [13,50,51]. Further,

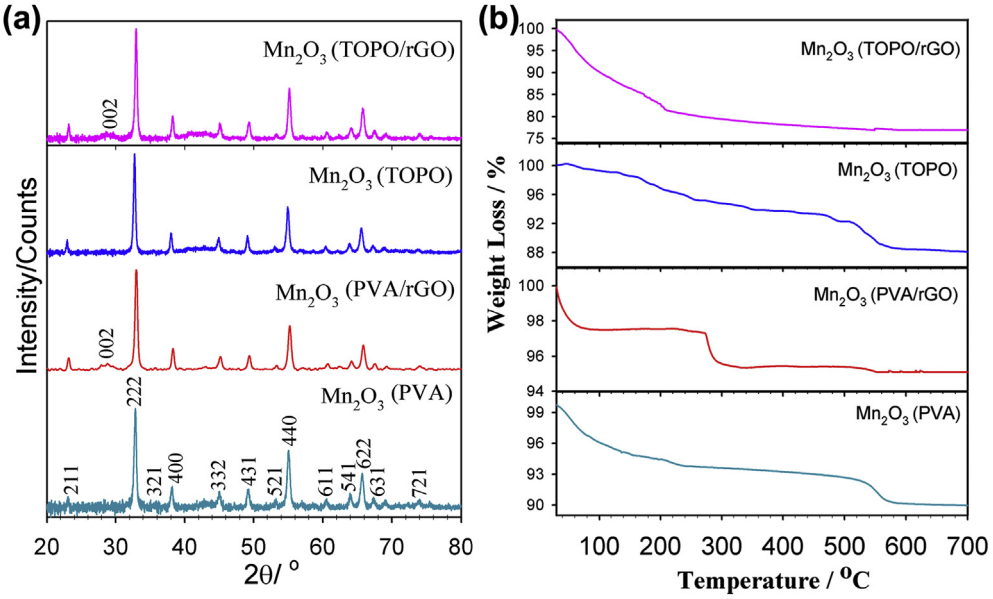

Fig. 1 – Structural characterization of Mn_2O_3 and graphene supported hierarchical Mn_2O_3. (a) XRD patterns of Mn_2O_3/PVA, Mn_2O_3/TOPO, Mn_2O_3/PVA/rGO and Mn_2O_3/TOPO/rGO. (b) Thermal gravimetric analysis (TGA) profiles of Mn_2O_3/PVA, Mn_2O_3/TOPO, Mn_2O_3/PVA/rGO and Mn_2O_3/TOPO/rGO.

the weight remains nearly unchanged suggests high thermal stability of the as prepared Mn_2O_3 (Fig. 1b). Similarly, graphene supported Mn_2O_3/PVA/rGO demonstrated high thermal stability with ~5% weight loss up to 800 °C. For, Mn_2O_3/TOPO/rGO, the weight loss of ~20–30% occurs between 200 and 280 °C may be associated with the decrease of labile oxygen-containing functional groups of rGO yielding CO, CO_2 and steam [52]. A residual mass of about 80–95% indicating loading of Mn_2O_3 oxides in the nanocomposites.

The structure and morphology of the as prepared Mn_2O_3 and Mn_2O_3/rGO composites were investigated by field-emission scanning electron microscopy (FESEM) and transmission electron microscopy (TEM). Fig. 2a and b illustrates the formation of hierarchical Mn_2O_3 microstructure in the range of 2.5–4 μm using PVA as a structure controlling agent without any support. The morphologies of the Mn_2O_3/PVA/rGO composites using PVA as controlling agent in presence of graphene oxides as support are shown in Fig. 2c and d. The flower-like Mn_2O_3 micro-spheres with size ~2 μm are anchored on graphene sheets are noticeably observed in Fig. 2c. Additionally, the Mn_2O_3 micro-spheres supported on graphene sheets exhibit partially overlapped and crumpled at many regions as shown in Fig. 2c. The low magnification SEM image (Fig. 2d) displays that the flower-like microspheres are constructed from numerous 2D nanoflakes with several tens of nanometers in thickness.

For Mn_2O_3 using TOPO as chelating ligand, SEM image (Fig. 3a and b) reveals rose-like characteristic which are assembled with ultrathin Mn_2O_3 with diameters in the range of 1.5 μm. When GO was predispersed in the reaction solution, the as prepared composites display a 3D architecture consisting of rGO nanosheets and Mn_2O_3 microstructure (Fig. 3c and d) with diameter of ~3.5 μm, also possess petal-like morphology composed of ultrathin Mn_2O_3 nanosheets as nanobuilding blocks.

From the high magnification SEM image (Fig. 3d) it can be clearly seen that the Mn_2O_3 with hierarchical flower structures formed with the rGO nanosheets. Such hierarchical flower-like micro-spheres appear to be suitable for catalytic applications. Energy Dispersive Spectrometer (EDS) pattern for the Mn_2O_3/TOPO shows the peaks of Mn and O further confirming the formation of Mn_2O_3 (Fig. S1). Further, the EDS elemental mapping clearly confirmed the presence and distribution of Mn, O, and C elements in the Mn_2O_3/TOPO/rGO as shown in Fig. 4. Quantitative EDS analysis confirms the formation of Mn_2O_3 in the composites as well as presence of graphene.

To reveal detailed microstructures and morphology of Mn_2O_3 and Mn_2O_3/rGO composites, transmission electron microscopy (TEM) and High Resolution TEM (HRTEM) was also employed (Figs. 5 and 6). Fig. 5a showed the formation of spherical type Mn_2O_3 with a mean diameter of 2.1 μm for

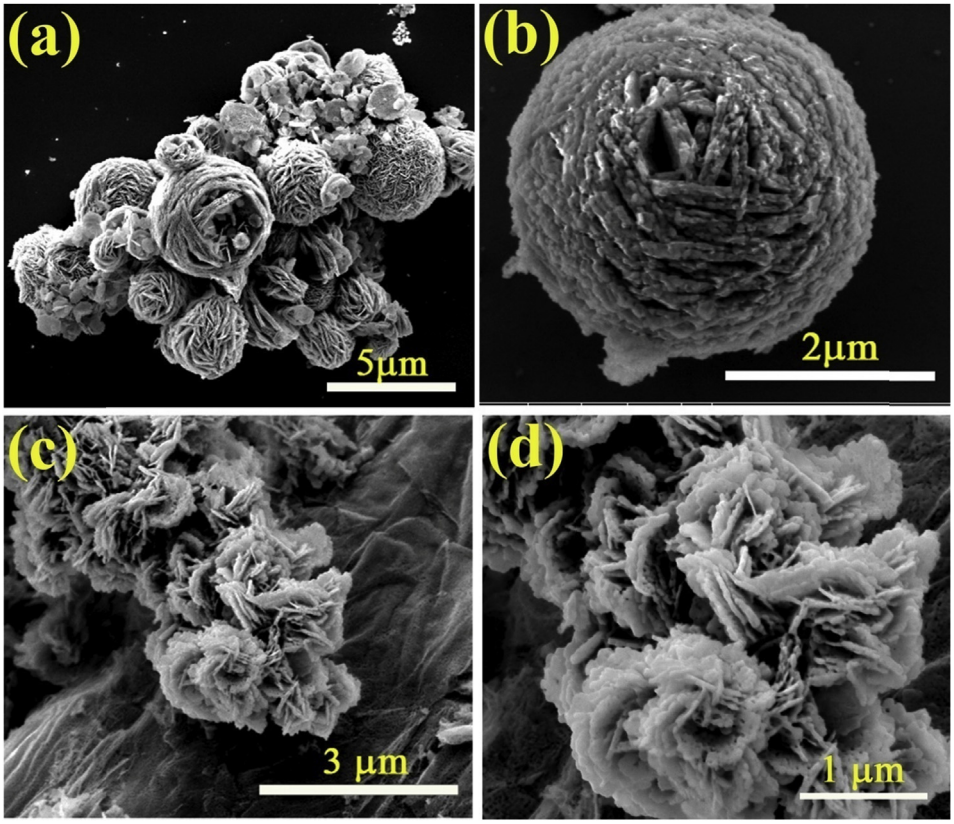

Fig. 2 – Scanning electron microscopy (SEM) images of Mn_2O_3 using PVA as structure controlling agent and graphene supported hierarchical Mn_2O_3 using PVA as structure controlling agent at different magnification. (a, b) Mn_2O_3/PVA, (c, d) Mn_2O_3/PVA/rGO.

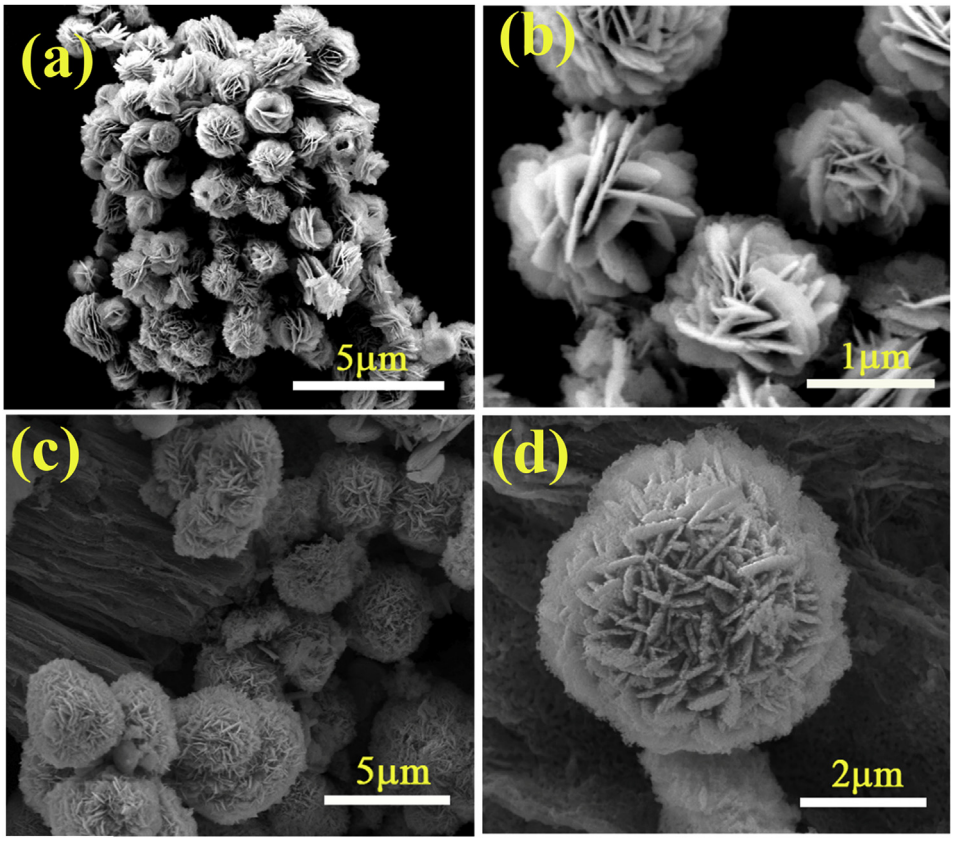

Fig. 3 – Scanning electron microscopy (SEM) images of Mn_2O_3 TOPO as structure controlling agent and graphene supported hierarchical Mn_2O_3 using TOPO as structure controlling agent at different magnification. (a, b) Mn_2O_3/TOPO and (c, d) Mn_2O_3/TOPO/rGO.

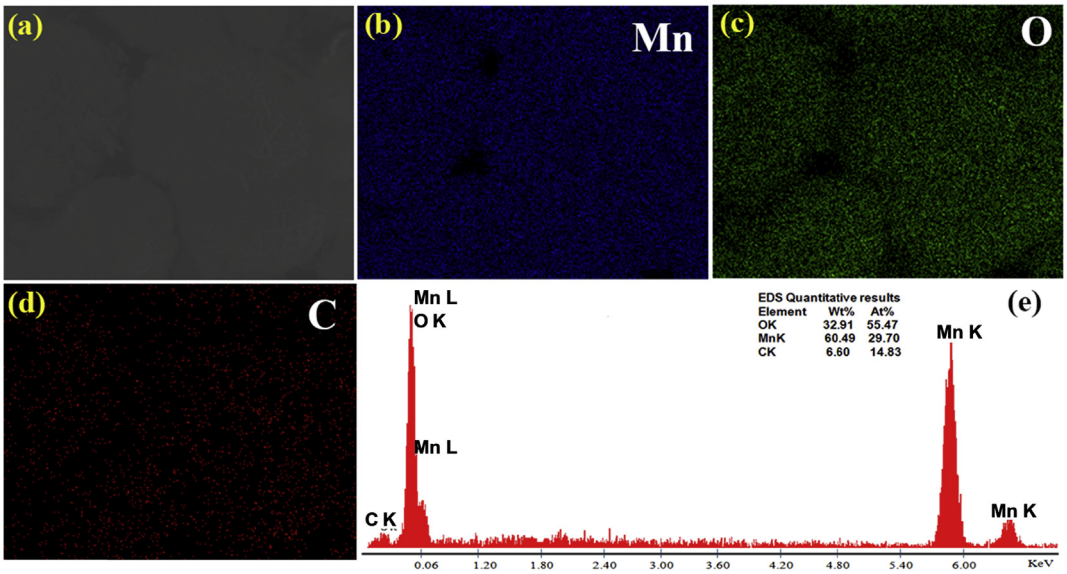

Fig. 4 – SEM images and elemental mapping of Mn_2O_3/TOPO/rGO. (a) SEM image (b) Mn, (c) O, (f) C elemental mapping and (d) EDS spectrum of Mn_2O_3/TOPO/rGO.

Mn_2O_3/PVA. A low magnification TEM image of Mn_2O_3/PVA shows that large scale microspheres which assembled by small particles are obtained (Fig. 5b), which is in agreement with the FESEM observations. As shown in Fig. 5c, the inter-planar distance between the fringes is found to be about 0.27 nm consistent with (222) planes of Mn_2O_3. Fig. 5d–f illustrates the TEM and HRTEM results for Mn_2O_3/PVA/rGO composites, from which the Mn_2O_3 formed a 3D

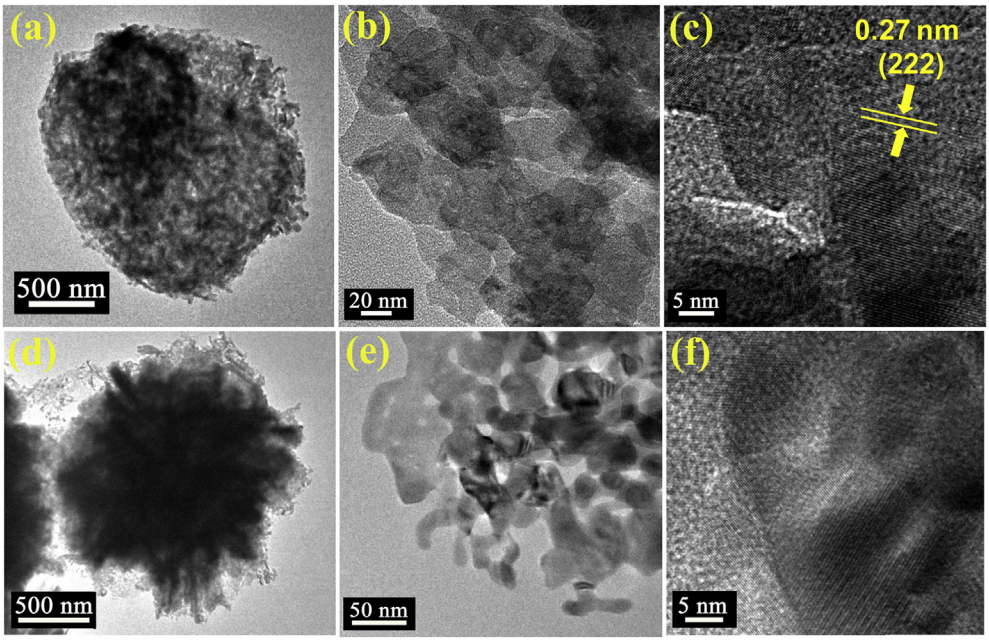

Fig. 5 – Transmission electron microscopy (TEM) images of Mn_2O_3/PVA and Mn_2O_3/PVA/rGO. (a), (b) TEM images at different magnification and (c) HRTEM image of Mn_2O_3/PVA. (d), (e) TEM images at different magnification and (f) HRTEM image of Mn_2O_3/PVA/rGO.

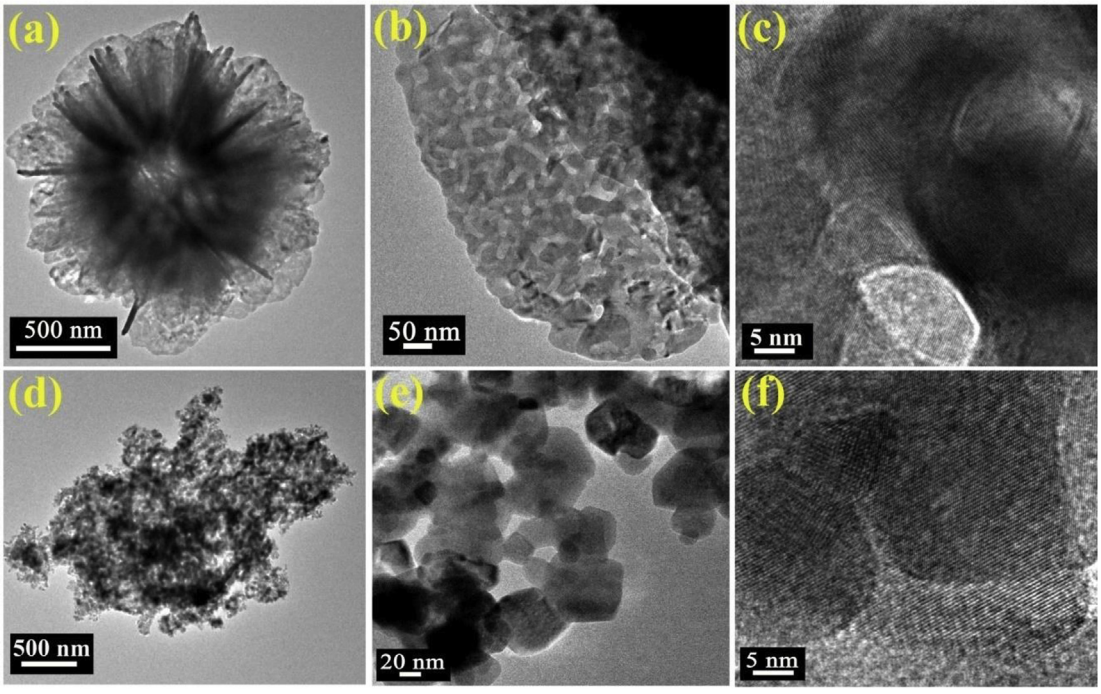

Fig. 6 – Transmission electron microscopy (TEM) images of Mn_2O_3/TOPO and Mn_2O_3/TOPO/rGO. (a), (b) TEM images at different magnification and (c) HRTEM image of Mn_2O_3/TOPO. (d), (e) TEM images at different magnification and (f) HRTEM image of Mn_2O_3/TOPO/rGO.

architecture of petal-like morphology with an average diameter of about 1.8 μm which is well consistent with those observed by SEM. The HRTEM image also demonstrated highly crystalline nature of Mn_2O_3/PVA/rGO with cubic phase (Fig. 5f).

As shown in Fig. 6a–c and d–f, the TEM images of Mn_2O_3/TOPO and Mn_2O_3/TOPO/rGO formed revealed flower-like morphology comprise a large number of thin nanosheets with an average diameter of 1.6 μm and aggregated microspheres with an average diameter of about 3 μm, respectively,

which is well consistent with those observed by SEM. The HRTEM images of the individual flower (Fig. 6b and c) and sphere (Fig. 6e and f) displayed well-resolved lattice planes with an inter-planar distance of 0.27 nm consistent with (222) planes of Mn_2O_3 which correspond to the cubic structure. However, it is difficult to observed graphene nanosheets in presence of assembled Mn_2O_3 structures in TEM images. This result obviously suggests that the preferential assembly of Mn_2O_3 in crystalline phase.

To investigate the effect of PVA and TOPO on the morphology of Mn_2O_3, the control experiments were operated without using TOPO and PVA while the other experimental parameters were maintained the same as aforementioned samples but produce irregular shape of manganese oxides (data not shown). On the other hand, irregular particle aggregates obtained in presence of graphene oxides without using capping agent under similar reaction condition also suggests significant role of PVA and TOPO as shown in Fig. S2. This suggests that the formation and morphology of the as prepared Mn_2O_3 strongly depended on the presence of TOPO, PVA and graphene oxides. PVA, a kind of nonionic surfactant, can physically absorb on the surface of manganese oxides subunits to control the grain growth and link the subunits to form a more stable morphology during the reaction process [5,53]. The particle growth in presence of TOPO is well controlled via lower intermolecular interaction which is differs significantly from the linear chain PVA ligand [54,55]. Generally, the growth process of crystals consists of two steps, an initial nucleating stage and a subsequent crystal growth process. At the nucleating stage, the crystalline phase of the seeds is critical for directing the intrinsic shapes of the crystals and Mn_2O_3 nuclei can form through the reaction between Mn^{2+} cations and O^- anions in the thermal process. At the subsequent step, the crystal growth stage strongly governs the final architecture of the crystals through the self-assembly of nanocrystals driven by the minimization of the surface energy which is consistent with the literature [56]. Moreover, higher supersaturation due to formation of large concentration of Mn_2O_3 nuclei causes the three-dimensional growth of preformed nuclei which leads to the formation of hierarchical structures which is common in the synthesis of inorganic nanomaterials [57].

Catalytic activity

Manganese oxides have been identified as one of excellent candidates as cathode material. In the present case, the electrochemical ORR and OER tests are performed using three-electrode system in the alkaline condition. The morphology controllable preparation of Mn_2O_3 allows a systematical investigation of their structure–performance relationship towards the oxygen reduction and evolution electrocatalysis. Cyclic voltammetry (CV) curves (Fig. S3) were found to exhibit oxygen reduction peaks for all the Mn_2O_3 electrodes in O_2-saturated KOH solution, but not the N_2-saturated KOH solution. Fig. 7a shows the ORR catalytic properties of the nanocrystalline Mn_2O_3 supported on rotating ring disk electrodes (RRDE) and the polarization profiles display typical ORR current–potential response. The key performance parameters such as onset potential, half-wave potential, kinetic current density and transferred electron transfer number of Mn_2O_3 have been summarized in Table 1. To evaluate the OER activity, cyclic voltammetry of Mn_2O_3 on glassy carbon electrodes was performed in N_2-saturated 0.1 M KOH solution (Fig. S4). The anodic current started at 0.6 V (vs. Ag/AgCl/sat.KCl) with a maximum current density in the range of 7–11 mA cm^{-2} at 1 V. As can be seen, the Mn_2O_3/TOPO/rGO has the highest electrocatalytic activity of all the aforementioned Mn_2O_3 catalysts in terms of both the onset potential and limiting current, highlighting the importance of the graphene support both for ORR and OER (Fig. 7b). The current density of Mn_2O_3/PVA/rGO slightly lower than that of Mn_2O_3/PVA, however, a significant low onset potential for Mn_2O_3/PVA/rGO justify the superior catalytic activity. The catalytic activity for ORR follow an order, Mn_2O_3/TOPO/rGO > Mn_2O_3/PVA > Mn_2O_3/PVA/rGO > Mn_2O_3/TOPO based on current density. However, the reason behind lower ORR catalytic activity of Mn_2O_3/PVA/rGO is not clear. On the other hand, the catalytic activity for OER is as follows: Mn_2O_3/TOPO/rGO > Mn_2O_3/PVA/rGO > Mn_2O_3/TOPO > Mn_2O_3/PVA. For graphene supported Mn_2O_3 electrocatalysts, presence of graphene nanosheets allow the effective dispersion as well as act as anchoring sites for the Mn_2O_3 NPs. Moreover, graphene nanosheets having holes, carbon vacancies, oxygen, and defects due to partial oxidation may generates additional chemically active sites for catalytic reactions which cause enhanced OER activity.

Further, with the increase of rotation rate, mass transport at the electrode surface improves, leading to the enhancement of current density (from 9.18 to 11.2 mA cm^{-2}) for ORR (Fig. 7c). The similar trend has been observed for all other Mn_2O_3 catalysts (Fig. S5). A comparative Table S1 has been added in SI which provide the comparison (e.g. in terms of catalytic activity) of the synthesized Mn_2O_3 to the similar work done in the same field.

Moreover, evaluation of the ORR catalytic behaviors is studied by determining the transferred electron number (n). From the Koutecky–Levich plot analysis, the value of n was found to 3.99, which is close to the theoretical value for $4e^-$ reduction of O_2 as shown in Fig. 7d. The other Mn_2O_3 catalyst the value of n was found to be in the range in the range of 3.4–3.9. During the ORR electrocatalysis on transition metal oxides under alkaline media, involve multistep steps of O_2 adsorption, formation of peroxide intermediate and further reduction or decomposition of peroxide to OH^- ions [58]. These processes are mediated by electron transfer, redox reactions and the surface oxygen adsorption ability that can be tuned by electronic structure [59].

One of the practical issues concerning stability of electrocatalysts can be studied by Chronoamperometry (CA) measurement, where the current at a constant applied voltage is recorded during an appropriate time period under working conditions.

For ORR, Mn_2O_3/TOPO/rGO electrode shows excellent durability with no obvious activity decay compared with the initial value over 10,000 s of continuous operation at a constant potential of −0.4 V as shown in Fig. 8a. Similarly, Mn_2O_3/PVA/rGO also shows ~10% but more than ~70% decay observed for Mn_2O_3/PVA suggests rGO play an important role as a support (Fig. S6a). For OER, Mn_2O_3/PVA/rGO catalysts, initially exhibited

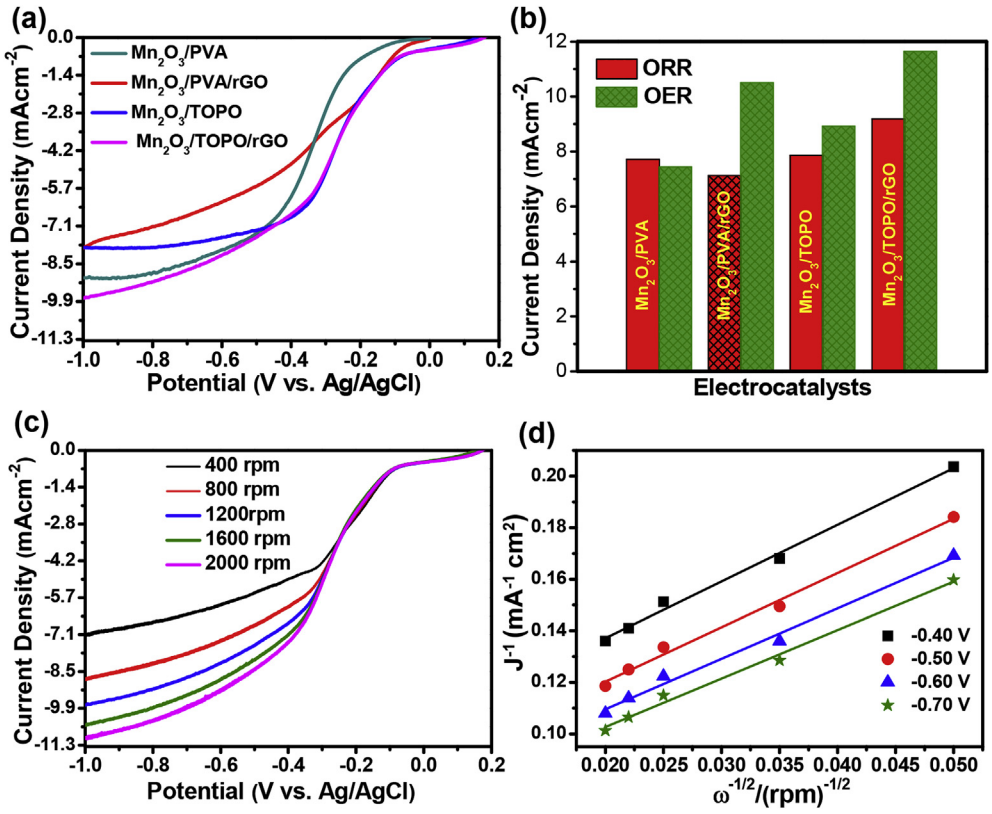

Fig. 7 – Electrocatalytic activities for ORR and OER. (a) Linear scan voltammogram (LSV) curves for Mn_2O_3/PVA, Mn_2O_3/TOPO, Mn_2O_3/PVA/rGO and Mn_2O_3/TOPO/rGO at an RDE (1200 rpm) in O_2-saturated 0.1 M KOH solution. Scan rate, 5 mV s^{-1}. (b) Comparative kinetic current of various samples for both O_2 reduction at 0.8 V at the RRDE measurements (1200 rpm) and evolution OER at 1.0 V, showing the electrocatalytic activities towards both ORR and OER. (c) LSV curves of Mn_2O_3/TOPO/rGO in oxygen-saturated 0.1 M KOH at various rotating speeds. (d) K–L plots for Mn_2O_3/TOPO/rGO at various potentials.

Table 1 – Comparison of the electrochemical performance of Mn_2O_3 electrocatalysts for ORR.

Electrode	Onset potential V/Ag/AgCl	No. e– from KL plot	Half-wave potential ($E_{1/2}$) (V)	J/mA $cm^{-2}_{(geom.)}$ @1200 rpm and –0.8 V	MA (mA/mg) @ –0.8 V vs Ag/AgCl
Mn_2O_3/PVA	–0.15	3.91	–0.34	8.82	31.1
Mn_2O_3/PVA/rGO	–0.08	3.75	–0.26	7.11	25.1
Mn_2O_3/TOPO	–0.04	3.42	–0.22	7.86	27.7
Mn_2O_3/TOPO/rGO	–0.09	3.99	–0.24	9.18	32.4

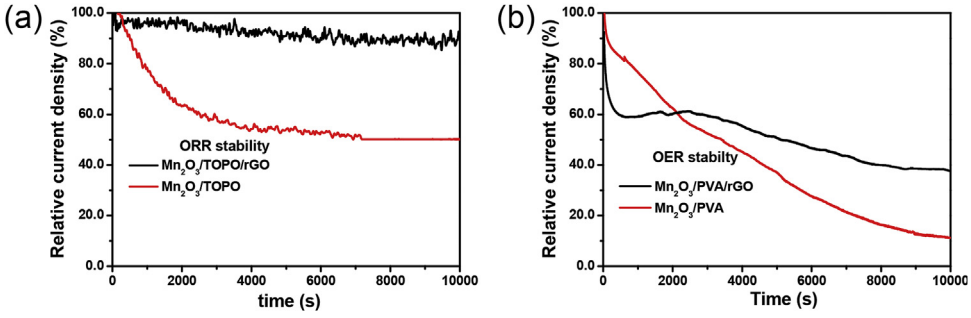

Fig. 8 – Stability of Mn_2O_3 for oxygen reduction reaction (ORR) and Oxygen evolution reaction (OER). Chronoamperometry curves for the (a) ORR of Mn_2O_3/TOPO (red curve), and Mn_2O_3/TOPO/rGO (black curve) and (b) OER of Mn_2O_3/PVA (red curve), Mn_2O_3/PVA/rGO (black curve), under 0.1 M KOH with scan rate 20 mV S^{-1}. (For interpretation of the references to colour in this figure legend, the reader is referred to the web version of this article.)

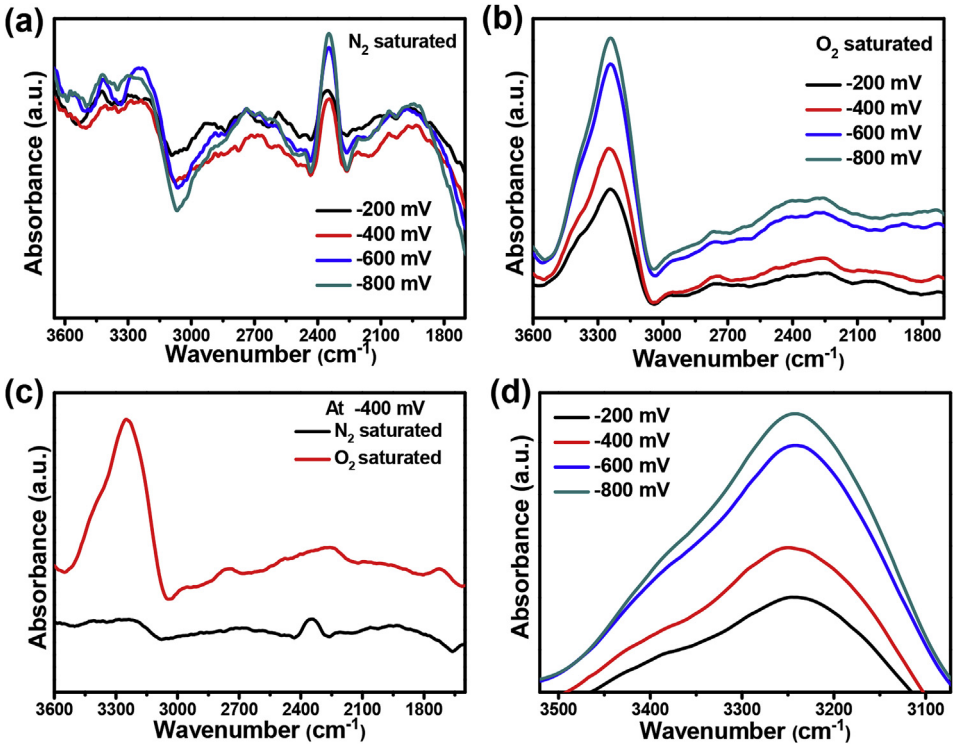

Fig. 9 – In-situ FTIR spectra for oxygen reduction reaction (ORR) using Mn_2O_3/TOPO/rGO as catalyst (a) in N_2 saturated, (b) in O_2 saturated, (c) comparative study in N_2 and O_2 and (d) enlarged portion of ν_{O-H} stretching frequency.

a current decay, which could be caused by partially block the active sites of the electrode due to accumulation of gas bubbles. The current density decayed in the first 80 s and attained a steady state thereafter, indicating that these Mn_2O_3 exhibit stable electrocatalytic performance towards OER (Fig. 8b). In contrast, for Mn_2O_3/PVA, pronounced current decay observed with almost 90% current decay. Hence, graphene supported Mn_2O_3 catalyst exhibits good stability in the alkaline solutions, which is important factor for energy conversion systems. For OER, Mn_2O_3/TOPO/rGO is followed similar trend with slightly better stability that Mn_2O_3/TOPO (Fig. S6).

Further, GCE was coated with the catalyst ink and in-situ study was performed with N_2 saturated as well as O_2 saturated electrolyte solution with varying applied potential from −200 mV to −800 mV, exactly the region where linear sweep voltammetry for ORR is recorded.

It is evident from Fig. 9a, there is no significant O–H stretching peak range from 3100 to 3350 cm^{-1} in N_2 saturated solution. Whereas in O_2 saturated solution, a strong peak for O–H stretch is observed prominently (Fig. 9b). This O–H stretching peak corresponds to water generated during oxygen reduction reaction on catalyst coated glassy carbon electrode surface [59]. In the Fig. 9c, a comparative plot is shown which clearly differentiate that there is ORR process occurring in O_2 saturated solution whereas there is no O–H peak in N_2 saturated solution. Furthermore, an enlarged portion of O–H stretching frequency in O_2 is shown in Fig. 9d. From Fig. 9d, it is observed that with increasing negative potential from −200 mV to −800 mV, the O–H absorption peak is getting more intense. This can be explained as, with increasing potential higher amount of water is produced i. e. diffusion of oxygen is higher on electrode surface at −800 mV comparative O_2 diffusion is lower at −200 mV. Linear sweep voltammetry supports this explanation as with increasing negative potential from −800 mV to −200 mV a higher current density is obtained i.e. diffusion of O_2 is higher.

Conclusion

A facile one-pot thermal reduction strategy was employed to fabricate hierarchical flower like manganese oxide and graphene–manganese oxide nanocomposites using PVA, TOPO and graphene oxide as precursors. The manganese oxide and graphene–manganese oxide nanocomposites demonstrated superior and stable electrocatalytic activity with high current density both for ORR and OER. It is suggested that the good electrochemical performance can be attributed to the 3D assembled hierarchical architecture and the presence of rGO network. In-situ FTIR study can monitor the adsorbed reaction intermediate of hydroxyl bands as a function of potential under ORR conditions. This facile and efficient reduction approach via hydrothermal process, cheapness, and availability of raw materials, without the need of template further can be extended to other metal oxides preparation and suitable for industrial manufacturing in scaled-up process. Moreover, the compositions of catalysts can be widely adjusted, which opens up new avenues in the effective

application of graphene nanosheet-supported metal oxides as promising electrode materials in near future.

Acknowledgements

P. K. and N.B. thanks the Council of Scientific and Industrial Research (CSIR, India) for fellowships. We thank the Department of Science and Technology (DST, India) for financial grants DST/TM/SERI/2k11/103 and SB/S1/PC-011/2013.

Appendix A. Supplementary data

Supplementary data related to this article can be found at http://dx.doi.org/10.1016/j.ijhydene.2016.12.008.

REFERENCES

[1] Jacobson MZ, Colella WG, Golden DM. Cleaning the air and improving health with hydrogen fuel-cell vehicles. Science 2005;308:1901–5.
[2] Steele BC, Heinzel A. Materials for fuel-cell technologies. Nature 2001;414:345–52.
[3] Debe MK. Electrocatalyst approaches and challenges for automotive fuel cells. Nature 2012;486:43–51.
[4] Zhang K, Han X, Hu Z, Zhang X, Tao Z, Chen J. Nanostructured Mn-based oxides for electrochemical energy storage and conversion. Chem Soc Rev 2015;44:699–728.
[5] Verma A, Jha AK, Basu S. Manganese dioxide as a cathode catalyst for a direct alcohol or sodium borohydride fuel cell with a flowing alkaline electrolyte. J Power Sources 2005;141:30–4.
[6] Cai Z, Xu L, Yan M, Han C, He L, Hercule KM, et al. Manganese oxide/carbon yolk-shell nanorod anodes for high capacity lithium batteries. Nano Lett 2015;15:738–44.
[7] Cao J, Zhu Y, Bao K, Shi L, Liu S, Qian Y. Microscale Mn_2O_3 hollow structures: sphere, cube, ellipsoid, dumbbell, and their phenol adsorption properties. J Phys Chem C 2009;113:17755–60.
[8] Rahaman H, Laha RM, Maiti DK, Ghosh SK. Fabrication of Mn_2O_3 nanorods: an efficient catalyst for selective transformation of alcohols to aldehydes. RSC Adv 2015;5:33923–9.
[9] Salazar-Alvarez G, Sort J, Suriñach S, Baró MD, Nogués J. Synthesis and size-dependent exchange bias in inverted core-shell MnO/Mn_3O_4 nanoparticles. J Am Chem Soc 2007;129:9102–8.
[10] Yang G, Yan W, Wang J, Yang H. Fabrication and formation mechanism of Mn_2O_3 hollow nanofibers by single-spinneret electrospinning. CrystEngComm 2014;16:6907–13.
[11] Zhang Y, Yan Y, Wang X, Li G, Deng D, Jiang L, et al. Facile synthesis of porous Mn_2O_3 nanoplates and their electrochemical behaviour as anode materials for lithium ion batteries. Chem Eur J 2014;20:6126–30.
[12] Li Q, Yin L, Li Z, Wang X, Qi Y, Ma J. Copper doped hollow structured manganese oxide mesocrystals with controlled phase structure and morphology as anode materials for lithium ion battery with improved electrochemical performance. ACS Appl Mater Interfaces 2013;5:10975–84.
[13] Kar P, Sardar S, Ghosh S, Parida MR, Liu B, Mohammed OF, et al. Nano surface engineering of Mn_2O_3 for potential light-harvesting application. J Mater Chem 2015;3:8200–11.
[14] Poyraz A, Kuo CH, Biswas S, King'ondu CK, Suib SL. A general approach to crystalline and monomodal pore size mesoporous materials. Nat Commun 2013;4:1–10.
[15] Cheng J, Che R, Liang C, Liu J, Wang M, Xu J. Hierarchical hollow $Li_4Ti_5O_{12}$ urchin-like microspheres with ultra-high specific surface area for high rate lithium ion batteries. Nano Res 2014;7:1043–53.
[16] Kao J, Thorkelsson K, Bai P, Rancatore BJ, Xu T. Toward functional nanocomposites: taking the best of nanoparticles, polymers, and small molecules. Chem Soc Rev 2013;42:2654–78.
[17] Zhang L, Wu HB, Madhavi S, Hng HH, Lou XW. Formation of Fe_2O_3 microboxes with hierarchical shell structures from metal-organic frameworks and their lithium storage properties. J Am Chem Soc 2012;134:17388–91.
[18] Duan J, Chen S, Dai S, Qiao SZ. Shape control of Mn_3O_4 nanoparticles on nitrogen-doped graphene for enhanced oxygen reduction activity. Adv Funct Mater 2014;14:2072–8.
[19] Cheng Y, Fan Y, Pei Y, Qiao M. Graphene-supported metal/metal oxide nanohybrids: synthesis and applications in heterogeneous catalysis. Catal Sci Technol 2015;5:3903–16.
[20] Mette K, Bergmann A, Tessonnier JP, Hävecker M, Yao L, Ressler T, et al. Nanostructured manganese oxide supported on carbon nanotubes for electrocatalytic water splitting. ChemCatChem 2012;4:851–62.
[21] Reddy AL, Shaijumon MM, Gowda SR, Ajayan PM. Coaxial MnO_2/carbon nanotube array electrodes for high-performance lithium batteries. Nano Lett 2009;9:1002–6.
[22] Kwon OS, Kim T, Lee JS, Park SJ, Park HW, Kang M, et al. Fabrication of graphene sheets intercalated with manganese oxide/carbon nanofibers: toward high-capacity energy storage. Small 2013;9:248–54.
[23] Yu D, Goh K, Wang H, Wei L, Jiang W, Zhang Q, et al. Scalable synthesis of hierarchically structured carbon nanotube-graphene fibres for capacitive energy storage. Nat Nanotech 2014;9:555–62.
[24] Ghosh S, Teillout AL, Floresyona D, de Oliveira P, Hagège A, Remita H. Conducting polymer-supported palladium nanoplates for applications in direct alcohol oxidation. Int J Hydrogen Energy 2015;40:4951–9.
[25] El-Kady MF, Strong V, Dubin S, Kaner RB. Laser scribing of high-performance and flexible graphene-based electrochemical capacitors. Science 2012;335:1326–30.
[26] Ghosh S, Remita H, Kar P, Choudhury S, Sardar S, Beaunier P, et al. Facile synthesis of Pd nanostructures in hexagonal mesophases as a promising electrocatalyst for ethanol oxidation. J Mater Chem A 2015;3:9517–27.
[27] Xia BY, Yan Y, Wang X, Lou (David) XW. Recent progress on graphene-based hybrid electrocatalysts. Mater Horiz 2014;1:379.
[28] Wang L, Yin F, Yao C. N-doped graphene as a bifunctional electrocatalyst for oxygen reduction and oxygen evolution reactions in an alkaline electrolyte. Int J Hydrogen Energy 2014;39:15913–9.
[29] Ghosh S, Kar P, Bhandary N, Basu S, Sardar S, Maiyalagan T, et al. Microwave-assisted synthesis of porous Mn_2O_3 nanoballs as bifunctional electrocatalyst for oxygen reduction and evolution reaction. Catal Sci Tech 2016;6:1417–29.
[30] Gorlin Y, Lassalle-Kaiser B, Benck JD, Gul S, Webb SM, Yachandra VK, et al. In situ X-ray absorption spectroscopy investigation of a bifunctional manganese oxide catalyst with high activity for electrochemical water oxidation and oxygen reduction. J Am Chem Soc 2013;135:8525–34.
[31] Prabu M, Ramakrishnan P, Ganesan P, Manthiram A, Shanmugam S. $LaTi_{0.65}Fe_{0.35}O_{3-\delta}$ nanoparticle-decorated nitrogen-doped carbon nanorods as an advanced hierarchical air electrode for rechargeable metal-air batteries. Nano Energy 2015;15:92–103.

[32] Ganesan M, Prabu M, Sanetuntikul J, Shanmugam S. Cobalt sulfide nanoparticles grown on nitrogen and sulfur codoped graphene oxide: an efficient electrocatalyst for oxygen reduction and evolution reactions. ACS Catal 2015;5:3625–37.
[33] Maiyalagan T, Jarvis KA, Therese S, Ferreira PJ, Manthiram A. Spinel-type lithium cobalt oxide as a bifunctional electrocatalyst for the oxygen evolution and oxygen reduction reactions. Nat Commun 2014;5:1–8.
[34] Liang Y, Li Y, Wang H, Zhou J, Wang J, Regier T, et al. Co_3O_4 nanocrystals on graphene as a synergistic catalyst for oxygen reduction reaction. Nat Mater 2011;10:780–6.
[35] Lee T, Jeon EK, Kim BS. Mussel-inspired nitrogen-doped graphene nanosheet supported manganese oxide nanowires as highly efficient electrocatalysts for oxygen reduction reaction. J Mater Chem A 2014;2:6167–73.
[36] Kumar K, Canaff C, Rousseau J, Arrii-Clacens S, Napporn TW, Habrioux A, et al. Effect of the oxide–carbon heterointerface on the activity of Co_3O_4/NRGO nanocomposites toward ORR and OER. J Phys Chem C 2016;120:7949–58.
[37] Prabu M, Ramakrishnan P, Shanmugam S. $CoMn_2O_4$ nanoparticles anchored on nitrogen-doped graphene nanosheets as bifunctional electrocatalyst for rechargeable zinc–air battery. Electrochem Commun 2014;41:59–63.
[38] Bian WY, Yang ZR, Strasser P, Yang RZ. A $CoFe_2O_4$/graphene nanohybrid as an efficient bi-functional electrocatalyst for oxygen reduction and oxygen evolution. J Power Sources 2014;250:196–203.
[39] Liu Y, Li J, Li W, Li Y, Chen Q, Liu Y. Spinel $LiMn_2O_4$ nanoparticles dispersed on nitrogen-doped reduced graphene oxide nanosheets as an efficient electrocatalyst for aluminium-air battery. Int J Hydrogen Energy 2015;40:9225–34.
[40] Zhao M, Li X, Song L, He D, Zhang Z. Substrate-assisted deposition of metal oxides on three-dimensional porous reduced graphene oxide networks as bifunctional hybrid electrocatalysts for the oxygen evolution and oxygen reduction reactions. ChemCatChem 2016;8:2808–16.
[41] Lu H, Yan J, Zhang Y, Huang Y, Gao W, Fan W, et al. In situ growth of Co_3O_4 nanoparticles on interconnected nitrogen-doped graphene nanoribbons as efficient oxygen reduction reaction catalyst. ChemNanoMat 2016;2:972–9.
[42] Xia WY, Li1 Nan, Li QY, Ye KH, Xu CW. Au-$NiCo_2O_4$ supported on threedimensional hierarchical porous graphene-like material for highly effective oxygen evolution reaction. Sci Rep 2016;6:23398.
[43] Kannan R, Kim AR, Kim JS, Yoo DJ. 3D graphene-mixed metal oxide-supported carbon palladium quantum dot nanoarchitectures–A facile bifunctional electrocatalyst for direct ethylene glycol fuel cells and oxygen evolution reactions. Int J Hydrogen Energy 2016;41:18033–43.
[44] Wen C, Gao X, Huang T, Wu X, Xu L, Yu J, et al. Reduced graphene oxide supported chromium oxide hybrid as high efficient catalyst for oxygen reduction reaction. Int J Hydrogen Energy 2016;41:11099–107.
[45] Hong WT, Risch M, Stoerzinger KA, Grimaud A, Suntivich J, Shao-Horn Y. Toward the rational design of non-precious transition metal oxides for oxygen electrocatalysis. Energy Environ Sci 2015;8:1404–27.
[46] Lee JS, Lee T, Song HK, Cho J, Kim BS. Ionic liquid modified graphene nanosheets anchoring manganese oxides nanoparticles as efficient electrocatalysts for Zn-air batteries. Energy Environ Sci 2011;4:4148–54.
[47] Duan J, Zheng Y, Chen S, Tang Y, Jaroniec M, Qiao S. Mesoporous hybrid material composed of Mn_3O_4 nanoparticles on nitrogen-doped graphene for highly efficient oxygen reduction reaction. Chem Commun 2013;49:7705–7.
[48] Hummers WS, Offeman RE. Preparation of graphitic oxide. J Am Chem Soc 1958;80:1339.
[49] Paulus UA, Schmidt TJ, Gasteiger HA, Behm RJ. Oxygen reduction on a high-surface area Pt:Vulcan carbon catalyst: a thin-film rotating ring-disk electrode study. J Electroanal Chem 2001;495:134–45.
[50] Fraioli AV. Investigation of manganese dioxide as an improved solid desiccant. Proc electrochem Soc 1985;85:342–68.
[51] Qiu G, Huang H, Dharmarathna S, Benbow E, Stafford L, Suib SL. Hydrothermal synthesis of manganese oxide nanomaterials and their catalytic and electrochemical properties. Chem Mater 2011;23:3892–901.
[52] Stankovich S, Dikin DA, Piner RD, Kohlhaas KA, Kleinhammes A, Jia Y, et al. Synthesis of graphene-based nanosheets via chemical reduction of exfoliated graphite oxide. Carbon 2007;45:1558–65.
[53] Borah JP, Barman J, Sharma KC. Structural and optical properties of ZnS nanoparticles. Chalcogenide Lett 2008;5:201–8.
[54] Doan-Nguyen VVT, Carroll PJ, Murray CB. Structure determination and modeling of monoclinic trioctylphosphine oxide. Acta Crystallogr C 2015;71:239–41.
[55] Sadik PW, Pearton SJ, Norton DP, Lambers E, Ren F. Functionalizing Zn- and O-terminated ZnO with thiols. J Appl Phys 2007;10:104514.
[56] Cho KS, Talapin DV, Gaschler W, Murray CB. Designing PbSe nanowires and nanorings through oriented attachment of nanoparticles. J Am Chem Soc 2005;127:7140–7.
[57] Xi LF, Lam YM. Controlling growth of CdSe nanowires through ligand optimization. Chem Mater 2009;21:3710–8.
[58] Zhang J, Zhao Z, Xia Z, Dai L. A metal-free bifunctional electrocatalyst for oxygen reduction and oxygen evolution reactions. Nat Nanotechnol 2015;10:444–52.
[59] Kunimatsu K, Yoda KT, Tryk DA, Uchida M, Watanabe H. In situ ATR-FTIR study of oxygen reduction at the Pt/Nafion interface. Phys Chem Chem Phys 2010;12:621–9.